LETTER

Multimaterial Fibers with Nanoemitters Enable Conformal X-ray Imaging with 3D Printed and Woven Scintillators

Bedil M. Saidzhonov, Khursand E. Yorov, Peng Yuan, Saidkhodzha Nematulloev, Azimet Akber Karluk, Taimoor Ahmad, Omar F. Mohammed, Osman M. Bakr,* and Mehmet Bayindir*

Read Online

ACCESS | Metrics & More | Article Recommendations | SI Supporting Information

ABSTRACT: Multimaterial luminescent fibers featuring integrated organic, inorganic, or hybrid nanoemitters are essential elements within a multitude of photonic systems. These systems encompass critical applications, such as single photon sources, high-energy radiation and particle sensors, and wireless optical communication networks. However, the integration of highly efficient luminescent nanomaterials into fibers with predefined geometries, materials, and functionalities remains challenging. This work reports on a process for fabricating indefinitely long multimaterial polymer fibers that can be doped with different organic−inorganic hybrid emitters, such as $Cs_3Cu_2I_5$ nanoparticles, Cu_2I_2 nanoclusters, and Mn-doped $Cs_4CdBi_2Cl_{12}$ phosphors. This versatility allows for the creation of fibers with tunable emission colors, which enable the realization of large-area, high-performance scintillation surfaces by additive manufacturing, weaving, or rolling. These conformal scintillator screens have been used to demonstrate X-ray imaging of nonplanar complex shapes without the image distortion and resolution degradation associated with rigid planar scintillator configurations. Additive manufacturing of sophisticated three-dimensional scintillators with nanoemitters offers opportunities for personalized medical imaging platforms, particularly for breast cancer screening, as well as applications in large-area high-energy radiation and particle detection.

Multimaterial fibers with nanoemitters enable conformal X-ray scintillators

Visible / X-ray — 3D printed | Woven fabric | Roll-to-image
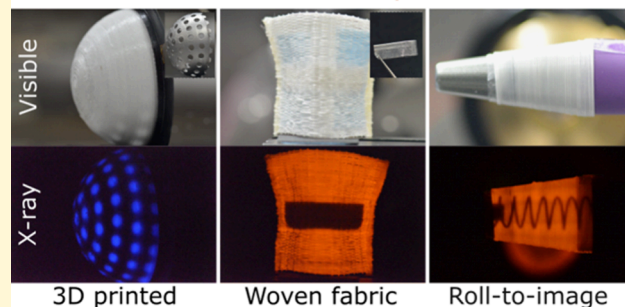
Since their first demonstration about 20 years ago, multimaterial fibers and in-fiber devices have unlocked unique opportunities for advancements across electronics, photonics, electromechanics, and optogenetics.[1−10] Luminescent multimaterial fibers with integrated nanoemitters are indispensable components of many photonic systems including single-photon sources for quantum information technologies, high-energy radiation (X-ray and γ-ray) and particle (α particle and cosmic ray) sensing and imaging, and wireless optical communications. However, the integration of highly efficient quantum emitters into fibers with predefined geometries and functionalities is still challenging. The introduction of highly stable and efficient organic, inorganic, or hybrid luminescent nanomaterials into a polymer matrix and the subsequent drawing of such multimaterial composites into functional flexible fibers offer opportunities for the emergence of the above-mentioned applications. In particular, the realization of highly efficient scintillation fibers opens new possibilities for constructing three-dimensional (3D) conformal X-ray imaging systems.

X-rays provide a unique opportunity for nondestructive and noninvasive testing due to their significant penetrability into the human body and other materials. Therefore, X-rays have been extensively used for medical diagnostics and therapy, industrial material testing, scientific research, and security inspection.[11−16] Among different X-ray device architectures, indirect flat-panel X-ray detectors are currently one of the most common in use.[11−13,17−21] These detectors usually consist of a planar scintillator coupled with an array of photodetectors.[22−24] Although flat-panel scintillation detectors can provide detailed two-dimensional projection images, these images often face distortion, because they are formed by
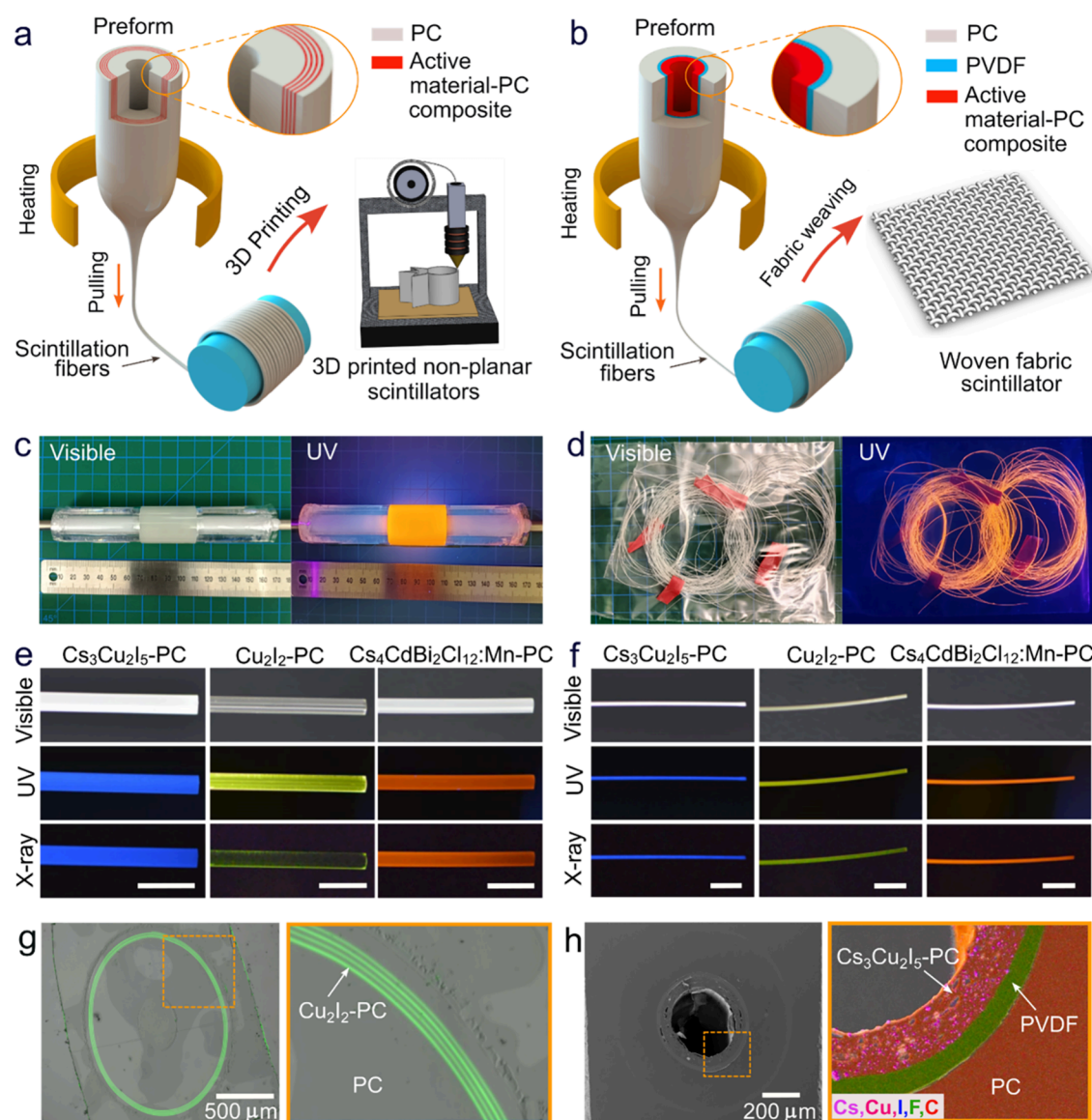
Figure 1. Production of multimaterial X-ray scintillation fibers. Schematic illustration of the preform structure and fiber drawing scheme for fibers designed for (a) additive manufacturing of 3D scintillators and (b) woven scintillation fabric production. (c) Photographs of a consolidated $Cs_4CdBi_2Cl_{12}$:Mn-PC preform under visible light and UV illumination. (d) $Cs_4CdBi_2Cl_{12}$:Mn-PC fibers under visible light and UV illumination. Images of the fibers designed for (e) additive manufacturing and (f) fabric production under visible light, UV and X-ray irradiation. Scale bars in panels (e) and (f) are 5 mm and 2 mm, respectively. (g) Fluorescence microscopy images of the cross-section of Cu_2I_2-PC fibers. (h) SEM (left) and elemental mapping (right) images of the cross-section of $Cs_3Cu_2I_5$-based fibers.

projecting three-dimensional objects onto a two-dimensional plane. Additionally, the uneven spatial distribution of X-ray dose and the unavoidable oblique incidence of X-rays on flat scintillation screens lead to a considerable reduction in image quality.[18,25,26] Obliquely incident X-rays on flat scintillation screens result in a significant decrease in the spatial resolution of X-ray images.[26] Consequently, planar scintillators cannot provide details on the actual shape, spatial location, and size of nonplanar objects, even though such details are crucial for medical diagnostics, therapy, and materials inspection.

Computed tomography can provide detailed information on objects of any shape, but it requires significantly longer X-ray exposure times (and dosages), which are known to increase cancer risk.[27] Computed tomography also requires costly and complicated device architectures and image processing compared to flat-panel X-ray detectors used in radiography.[17]

In this regard, X-ray imaging using a scintillator that closely matches the shape of the object being imaged, conformal imaging, can eliminate image distortion and give valuable insights into the actual structure, size, and location of the object. So far, nonplanar X-ray imaging systems have been limited to bendable scintillators[19,28−31] and direct detectors.[25,26,32] To the best of our knowledge, there have been no reports on the production of 3D scintillators with highly efficient quantum emitters of a given shape for conformal X-ray imaging.

In this work, we introduce scalable approaches to manufacture scintillators of arbitrary shapes for conformal X-ray imaging using polycarbonate/perovskite-related active material composite scintillation fibers. We demonstrate the integration of several X-ray active materials in the composite, namely, solution-processable $Cs_3Cu_2I_5$ nanoparticles, Cu_2I_2

nanoclusters, and $Cs_4CdBi_2Cl_{12}$:Mn phosphors. The transformation of composite multimaterial preforms into fibers by means of thermal drawing resulted in uniform scintillation fibers hundreds of meters long, without adversely affecting the X-ray active materials. The structure and dimensions of the fibers were then optimized to meet the requirements for additive manufacturing and woven fabric production. By using multilayered scintillation fibers as filaments for additive manufacturing, prototypes of 3D scintillators of different and complex shapes were successfully printed. Large-area flexible woven scintillation fabrics composed of cladding-free fibers were also successfully produced. The woven scintillation fabrics can be reversibly bent, stretched, and twisted, enabling their integration into 3D scintillators for conformal X-ray imaging. Conformal X-ray imaging with these 3D scintillators revealed their capability to serve as a hard-to-achieve imaging tool, offering precise information on the structure, shape, and dimensions of nonflat objects. The developed approaches, which are based on using inexpensive solution processable highly efficient X-ray active materials and scalable production technologies, provide a platform for manufacturing low-cost high-performance scintillators of arbitrary shapes and wearable scintillation fabrics important for the realization of personalized conformal X-ray imaging systems.

The selection of $Cs_3Cu_2I_5$ nanoparticles, $Cs_4CdBi_2Cl_{12}$:Mn microcrystals, and Cu_2I_2 nanoclusters as active materials was driven by their superior stability and unique photophysical properties, including high photoluminescence quantum yields (PLQY), large Stokes shifts, and high scintillation light yields (LYs). However, due to the compatibility of the polycarbonate (PC) matrix with various materials, the developed method can also be employed to incorporate other classes of materials, such as organic scintillators,[33−36] metal−organic frameworks,[37−40] and other inorganic scintillators,[41−44] into composite fibers, thereby expanding the range of potential applications.

The composite scintillation fibers described here were drawn from macroscopic preforms using the thermal size reduction technique.[3,4] As X-ray active materials, we selected several materials with different size regimes: a few atoms containing Cu_2I_2 nanoclusters, $Cs_3Cu_2I_5$ nanocrystals, and $Cs_4CdBi_2Cl_{12}$:Mn microcrystals. These materials were chosen to demonstrate the applicability of the developed methods to different material systems. In addition, these materials offer high scintillation LYs and easy solution-based synthesis.[14,28,45] The materials synthesis and characterization, preform preparation, and fiber drawing procedures are provided in the experimental section and Supporting Information (SI).

PC was used as the polymer matrix for the fabrication of both composite films and preforms. PC was selected for this role because of its relatively low glass-transition temperature (∼145 °C) and compatibility with numerous organic−inorganic low-dimensional materials. By maintaining consolidation and drawing temperatures at relatively low levels (186 and 215−270 °C, respectively), we successfully preserved the chemical and structural integrity of the active materials within the polymer matrix after drawing. Video S1 demonstrates a typical thermal drawing process of composite scintillation fibers.

Schematic diagrams depicting the preform architecture and fiber drawing procedures for additive manufacturing and woven fabric fabrication are presented in Figures 1a and 1b, respectively. Figure 1c showcases images of a consolidated

$Cs_4CdBi_2Cl_{12}$:Mn-PC preform for additive manufacturing. Figure 1d depicts optical images of $Cs_4CdBi_2Cl_{12}$:Mn-PC fibers for the production of woven fabric under visible light and UV illumination. Magnified images of all obtained fibers under visible light, UV, and X-ray irradiation are presented in Figures 1e and 1f. The fibers illustrated in Figure 1e possess a diameter of ∼1.7 mm and were designed for additive manufacturing. It is noteworthy that these fibers exhibit a hollow core and a multilayered active material configuration positioned near the fiber surface. The multilayered structure for the active material, with layers of active material separated by PC layers, was implemented to achieve compositional homogeneity of the fibers. The uniform color of the fibers under visible light, UV, and X-ray irradiation corroborates their compositional homogeneity. Photographs of the fibers designed for woven fabric production under visible light, UV, and X-ray irradiation are presented in Figure 1f. These fibers possess a hollow core surrounded by an active material. A thin layer of poly-(vinylidene fluoride) (PVDF) separates the active material from the outer thick PC layer, serving multiple purposes. First, the resistance of PVDF to most solvents enables selective etching of the external PC layer without disrupting the underlying active material, leading to the formation of thinner fibers composed primarily of the active composite material. This is crucial for achieving fabrics comprising predominantly active material with minimal inactive gaps between adjacent fibers. Second, due to PVDF's exceptional mechanical strength and toughness, the resulting fibers exhibit sufficient flexibility and resilience for fabric weaving. Third, PVDF's lower refractive index (n = 1.4) compared to the PC-composite (n ≈ 1.59) significantly enhances light extraction efficiency from the X-ray active layer. The fibers obtained in this study emit light under both X-ray and UV excitations, rendering them promising for applications beyond scintillation screens, including UV detectors and down-conversion LED devices.

A multimodal approach, including fluorescence spectroscopy, fluorescence microscopy (FM), and scanning electron microscopy (SEM) was used to characterize fiber composition and cross-sectional morphology. Fibers were sectioned by using an ultramicrotome for FM and SEM analyses. Figure 1g presents a fusion of bright-field and fluorescence images of a Cu_2I_2-PC fiber developed for additive manufacturing. The FM images reveal a layered structure of the active material, with individual layers separated by layers of PC. The uniform emission emanating from the active material layers confirms the preservation of the active material within the fibers, implying that the drawing processes do not induce substantial alterations in the composition and structure of the active material. SEM images and corresponding elemental mapping patterns of the cross-section of $Cs_3Cu_2I_5$-PC, Cu_2I_2-PC, and $Cs_4CdBi_2Cl_{12}$:Mn-PC fibers designed for additive manufacturing are presented in Figure S7. Corroborating the FM data, the fibers exhibit a circular cross-section and elemental mapping confirms that the active material is situated near the fiber surface and exhibits a layered structure. Uniformly distributed aggregates of small particles and microcrystals are discernible along the active material layers in the images of fibers doped with $Cs_3Cu_2I_5$ nanocrystals and $Cs_4CdBi_2Cl_{12}$:Mn microcrystals. Elemental mapping confirmed the presence of Cs, Cu, and I in fibers activated with $Cs_3Cu_2I_5$ nanoparticles; Cu and I in fibers activated with Cu_2I_2 nanoclusters; and Cs, Cd, Bi, Cl, and Mn in fibers containing $Cs_4CdBi_2Cl_{12}$:Mn microcrystals. All elements were uniformly distributed
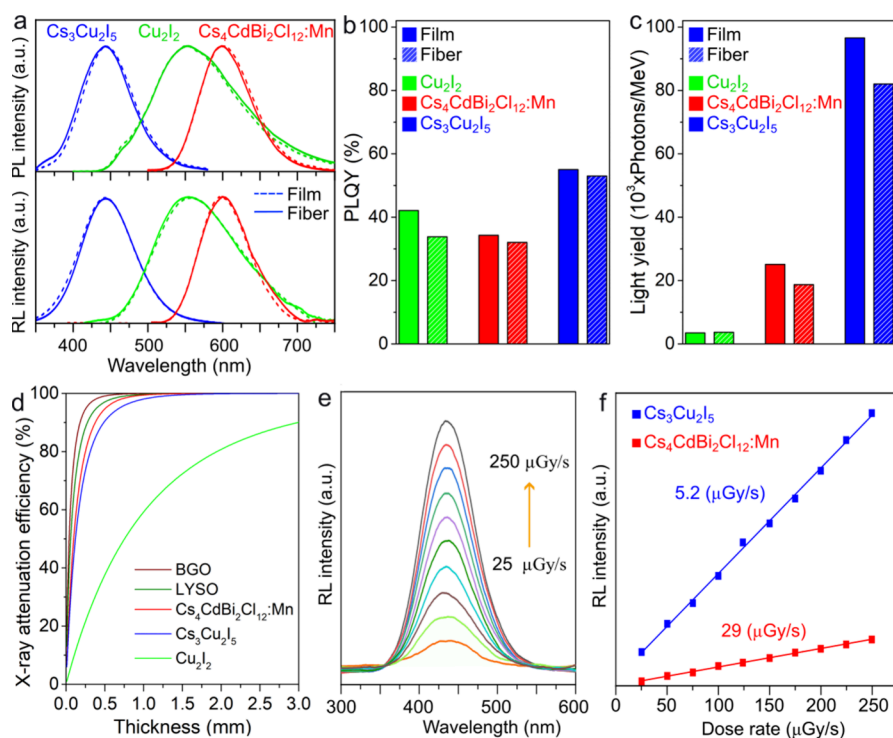
Figure 2. Optical and X-ray characterization of the scintillation films and fibers. (a) Photoluminescence (top) and radioluminescence (bottom) spectra of the composite films and fibers. (b) PLQY and (c) light yields of the composite films and fibers. (d) X-ray attenuation efficiencies as a function of scintillator thickness for Cu_2I_2 nanocluster, $Cs_3Cu_2I_5$, $Cs_4CdBi_2Cl_{12}$:Mn, and reference samples. (e) Radioluminescence spectrum of $Cs_3Cu_2I_5$-PC fibers under various X-ray excitation doses. (f) The dose dependency of the radioluminescence intensity for $Cs_3Cu_2I_5$-PC and $Cs_4CdBi_2Cl_{12}$:Mn-PC fibers.

throughout the active material layers, indicating a uniform fiber composition. This also suggests that the active material has a single-phase composition and that the fiber drawing processes did not alter the chemical composition of the active material. SEM images and elemental mapping patterns of the cross-section of $Cs_3Cu_2I_5$-PC, Cu_2I_2-PC, and $Cs_4CdBi_2Cl_{12}$:Mn-PC fibers designed for fabric production are presented in Figure 1h and Figure S7. According to the SEM images, the fibers have a circular cross-section and the active material, PVDF, and PC layers are sequentially arranged from the hollow core. Phase contrast between the active material, PVDF, and PC layers is clearly visible in the SEM images. Elemental mapping patterns revealed the presence of the elements constituting all of the phases. Additionally, the uniform spatial distribution of the elements in the active material layer suggests that the consolidation and drawing processes did not result in intermixing among the active composite, PVDF, and PC layers. The thin layer of PVDF separating the active material from the outer PC layer is distinctly evident in the elemental mapping patterns. The active composite and PVDF layers have average thicknesses of ∼90 and 18 μm, respectively, in fibers with a diameter of 400 μm.

Next, we investigated the photophysical properties of composite thin films and fibers doped with $Cs_3Cu_2I_5$ nanocrystals, Cu_2I_2 nanoclusters, and $Cs_4CdBi_2Cl_{12}$:Mn micro-crystals. Photoluminescence (PL) and radioluminescence (RL) spectra of the composite films and fibers are depicted in Figure 2a. The PL spectra reveal that both the composite films and fibers activated with $Cs_3Cu_2I_5$ nanocrystals, Cu_2I_2 nanoclusters, and $Cs_4CdBi_2Cl_{12}$:Mn microcrystals exhibit emission peaks centered at ∼444, 552, and 603 nm, respectively. These findings align well with previously reported PL spectra for

$Cs_3Cu_2I_5$ nanocrystals,[46] Cu_2I_2 nanoclusters,[47] and $Cs_4CdBi_2Cl_{12}$:Mn microcrystals.[48,49] The Cu_2I_2-PC composite exhibited a red-shifted emission by 18 nm compared with its bulk counterpart.[50] The position and full width at half-maximum (FWHM) of the emission peak of the fibers closely match those of the composite films. These results rule out any potential modifications in the composition and structure of the active material during the consolidation and fiber drawing procedures. Furthermore, the positions and FWHM of the RL peaks are similar to the corresponding PL results, and no substantial shifts between the RL and PL emission peaks were observed.

Figure 2b illustrates the evolution of the PLQY across the composite fiber fabrication process. Upon incorporation of Cu_2I_2 nanoclusters into the PC matrix, a substantial decrease in the PLQY is observed (from 91% to 42%). Conversely, the inclusion of $Cs_4CdBi_2Cl_{12}$:Mn microcrystals exhibits a minor reduction in the PLQY (from 41% to 34%), compared to the bulk material (Figure S8). Interestingly, the incorporation of $Cs_3Cu_2I_5$ nanoparticles into the PC matrix does not significantly impact their PLQY. Further fiber drawing using Cu_2I_2-PC composite films leads to a further PLQY decline (from 42% to 34%), indicating that high drawing temperatures can also influence the PLQY of Cu_2I_2-based composites. Similarly, the thermal drawing of $Cs_4CdBi_2Cl_{12}$Mn-based composite films induces a minor PLQY reduction (from 34% to 32%). Finally, the integration of $Cs_3Cu_2I_5$-based composite films into fibers results in a marginal PLQY decrease (from 55% to 53%). These results highlight the sensitivity of PLQY to the composite fabrication process and suggest that the incorporation of $Cs_3Cu_2I_5$ nanoparticles and $Cs_4CdBi_2Cl_{12}$:Mn microcrystals can mitigate PLQY losses during fiber drawing.
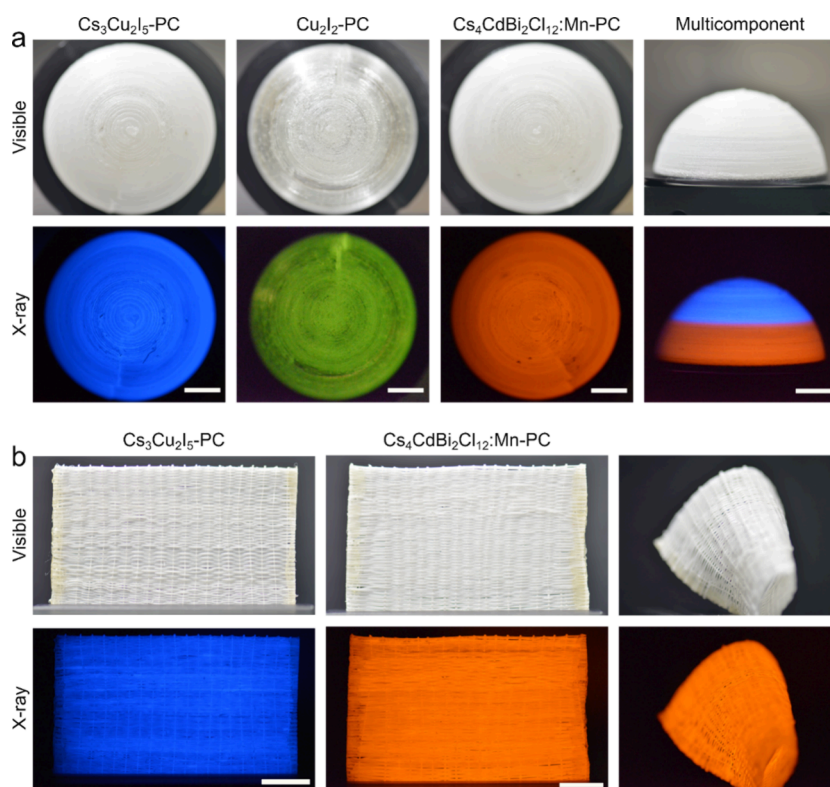
Figure 3. 3D-printed and woven fabric X-ray scintillators. (a) Photographs of single-component and multicomponent 3D-printed scintillators under visible light (top) and X-ray irradiation (bottom). (b) Images of $Cs_3Cu_2I_5$-PC and $Cs_4CdBi_2Cl_{12}$:Mn-PC-based woven scintillation fabrics under visible light (top) and X-ray irradiation (bottom). Scale bars are 1 cm in both panels (a) and (b).

The scintillation LYs of the composite films and fibers were measured by using a commercial BGO crystal as a reference (Figure 2c). The LY was determined based on the X-ray attenuation efficiency of the active material and its concentration within the composites (X-ray characterizations are detailed in the SI, section S8). Figure 2c shows the estimated LY for the composite films and fibers. The $Cs_3Cu_2I_5$-PC composite film exhibited a high scintillation LY of ∼97 000 photons/MeV. The subsequent drawing of the $Cs_3Cu_2I_5$-PC film produced composite fibers with an LY of ∼83 700 photons/MeV, a value comparable to that of pure $Cs_3Cu_2I_5$ nanoparticles (Figure S9).[45] The $Cs_4CdBi_2Cl_{12}$:Mn-PC composite film exhibited an LY of 25 100 photons/MeV, closely matching the LY of the bulk material (25 600 photons/MeV). Drawing the $Cs_4CdBi_2Cl_{12}$:Mn-PC film yielded composite fibers with an LY of 16 500 photons/MeV. The alteration in LY of $Cs_3Cu_2I_5$ and $Cs_4CdBi_2Cl_{12}$:Mn-PC-based composites during the drawing process is insignificant and parallels the modification in their PLQY. Despite exhibiting a high LY of ∼175 000 photons/MeV in crystalline powder form,[50] the Cu_2I_2-based composite films and fibers displayed a markedly low LY of ∼3000 photons/MeV. This substantial decrease in PLQY and LY compared to Cu_2I_2 crystalline powder is attributed to the gradual disappearance of aggregation-induced emission after dissolving nanoclusters in dichloromethane (DCM) prior to mixing with the PC matrix. We observed that the incorporation of nanoclusters into polymer matrices resulted in minimal changes to the PLQY and LY of fibers after high-temperature fiber drawing procedures.

Figure 2d illustrates the X-ray attenuation efficiencies, also known as stopping power, of $Cs_3Cu_2I_5$ nanocrystals, Cu_2I_2 nanoclusters, and $Cs_4CdBi_2Cl_{12}$:Mn microcrystals, in comparison to two commonly used scintillating crystals, LYSO:Ce and BGO. The X-ray stopping abilities of $Cs_3Cu_2I_5$ and $Cs_4CdBi_2Cl_{12}$:Mn are comparable to those of LYSO:Ce and BGO (Figure S10). This implies that these materials have similar stopping powers, which is a crucial factor for their potential applications in radiation detection.

Subsequently, we explored the correlation between the X-ray excitation dose and the RL of the scintillation fibers. Figure 2e depicts the dose dependency of the RL spectrum for fibers activated with $Cs_3Cu_2I_5$ nanocrystals. As the dose rate increases from 25 to 250 μGy/s, a significant enhancement in the RL intensity is observed. This dose-rate-dependent evolution of the RL spectrum was consistently observed for fibers activated with Cu_2I_2 nanoclusters and $Cs_4CdBi_2Cl_{12}$:Mn microcrystals. A strong linear correlation between the RL intensity and X-ray excitation dose was observed for all three samples (Figure 2f and Figure S12). The fibers activated with $Cs_3Cu_2I_5$ nanocrystals exhibited the lowest detection limit of 5.2 μGy/s, determined from the fitting line at a signal-to-noise ratio of 3. For the fibers activated with $Cs_4CdBi_2Cl_{12}$:Mn microcrystals and Cu_2I_2 nanoclusters, the detection limit was 29 and 340 μGy/s, respectively. The significantly higher detection limit for Cu_2I_2-based fibers is attributed to their reduced scintillation LY. The photophysical properties of few-atom Cu_2I_2 nanoclusters and other related structures are highly sensitive to their surroundings due to their extremely increased surface area and potential interactions through ligands.[47,51,52] These interactions between the polymer matrix and Cu_2I_2 nanoclusters likely contribute to the weak RL response of the Cu_2I_2-based composites.
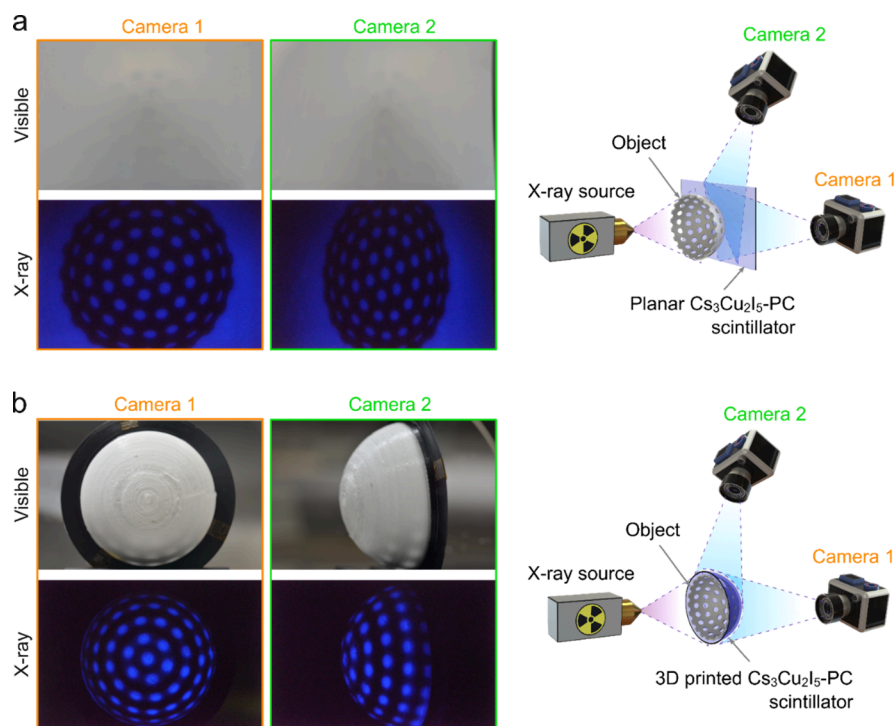
Figure 4. X-ray imaging with planar and conformal 3D-printed scintillators. (a) X-ray imaging using a planar $Cs_3Cu_2I_5$-PC scintillator. (b) Conformal X-ray imaging using a 3D-printed nonplanar $Cs_3Cu_2I_5$-PC scintillator. The schematic illustrations on the right side of panels (a) and (b) show the imaging setup and the relative positions of the object, scintillator, and cameras.

The spatial X-ray resolution of the scintillation fibers was evaluated by using a standard line-pair card (Figure S13). The spatial resolution of the fibers closely matches that of the corresponding composite films, demonstrating that the fiber drawing process has minimal effect on the resolution of the embedded scintillating particles. $Cs_3Cu_2I_5$-PC and Cu_2I_2-PC based fibers exhibited a high spatial resolution of 7.1 lp/mm, while $Cs_4CdBi_2Cl_{12}$:Mn-PC fibers displayed a lower resolution of 3.6 lp/mm. This difference in resolution is primarily due to the micrometer-sized $Cs_4CdBi_2Cl_{12}$:Mn particles employed in the $Cs_4CdBi_2Cl_{12}$:Mn-PC fibers, which cause significant light scattering and consequently reduce the spatial resolution.

Nonplanar X-ray scintillators with tailored geometries were fabricated utilizing well-established additive manufacturing methods.[53,54] The fiber drawing process was meticulously controlled by adjusting the furnace temperature, preform feed rate, and drawing speed to produce fibers of the desired diameters. This approach yielded uniform scintillation fibers with lengths of up to hundreds of meters and diameters ranging from 200 μm to 2 mm.

Multimaterial fibers containing active material multilayers with diameters ranging from 1.7 to 1.75 mm were identified as suitable for additive manufacturing using a commercially available 3D printer (see Video S2). A full description of the 3D printing process, along with optimized printing parameters, can be found in the SI. Figure S14a displays images of a roll of $Cs_4CdBi_2Cl_{12}$:Mn-PC fibers designed for additive manufacturing under visible light and UV irradiation, and a schematic of the 3D printing process is provided in Figure S14b. Using these scintillation fibers, a glove-shaped scintillator, a "scintillation" rabbit, and hemisphere-shaped scintillators were successfully fabricated (Figure 3a and Figure S14). In addition, the ability to modify the fiber composition during printing enabled the fabrication of multicomponent X-ray

scintillators. Photographs of single- and multicomponent hemispherical scintillators containing $Cs_3Cu_2I_5$ nanocrystals, Cu_2I_2 nanoclusters, and $Cs_4CdBi_2Cl_{12}$:Mn microcrystals as the active material under visible light and X-ray irradiation are shown in Figure 3a. As can be seen from these images, all of the fabricated scintillators have a well-defined shape with solid walls. The absence of gaps or voids in the printed structures confirms the suitability of composite fibers for 3D printing applications. This is further supported by the images of the printed scintillators under X-ray radiation, which show uniform emission throughout the scintillator volume. While the multicomponent X-ray scintillators appear nearly identical under visible light, their distinct emission colors allow for phase contrast under X-ray excitation. In addition, the interface between two distinct components of the multicomponent scintillator is clearly visible in the X-ray images, indicating that the printing process does not result in the mixing of the materials. The ability to fabricate multicomponent X-ray scintillators opens new avenues for manufacturing X-ray scintillators with sophisticated architectures including dual-energy X-ray detection systems. For dual-energy X-ray detectors comprising two different scintillators, the thickness of the individual scintillators must be optimized along with other parameters to achieve optimal imaging conditions.[55,56] Because 3D printing enables precise control over the size and shape during fabrication, we believe that the developed technique holds great promise for fabricating next-generation X-ray detectors with diverse architectures for medical diagnostics and industrial inspection.

Moreover, we explored the feasibility of utilizing multi-material scintillation fibers to fabricate scintillation fabrics, as X-ray active woven materials offer new prospects for nonplanar X-ray imaging due to their remarkable flexibility and stretchability.[57,58] Scintillation fibers with a diameter of 300−
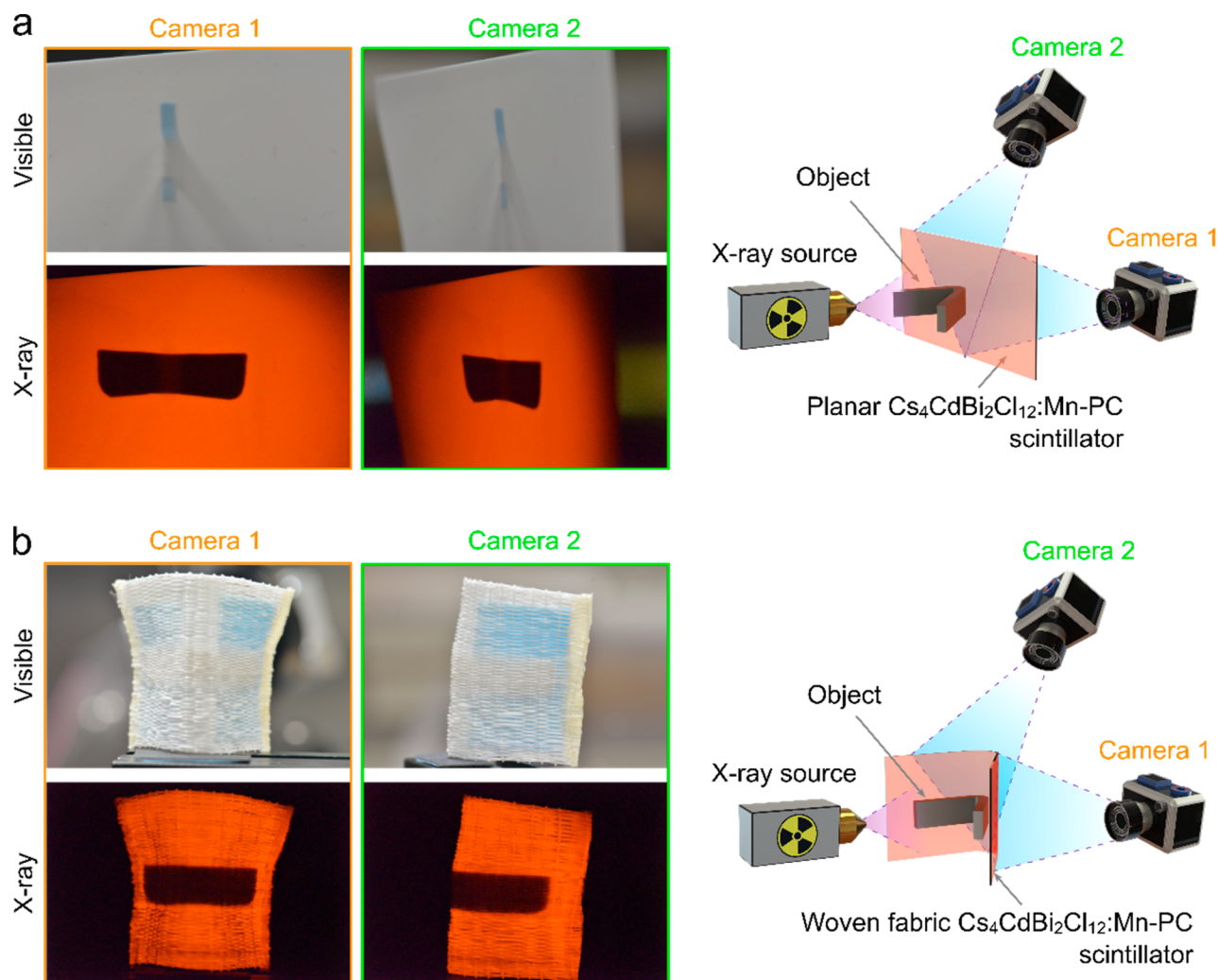
Figure 5. X-ray imaging with planar and flexible woven scintillators. (a) X-ray imaging using a planar $Cs_4CdBi_2Cl_{12}$:Mn-PC scintillator. (b) Conformal X-ray imaging using a woven $Cs_4CdBi_2Cl_{12}$:Mn-PC flexible scintillator. The right side of panels (a) and (b) demonstrate schematic illustrations of the imaging setup, as well as the positions of the object, scintillator, and cameras.

450 μm were chosen for fabric production, due to their superior flexibility.

Figure 1f shows digital images of fibers intended for woven fabric production. As can be seen in Figure 1b, these scintillation fibers possess a thick PC shell, which facilitates thin fiber drawing under the specified conditions. However, the direct weaving of such fibers results in scintillation fabrics with significant inactive gaps between adjacent fibers. To overcome this challenge, the outer PC shell of the fibers was etched in DCM (Figure S15). Etching the fibers in DCM for 10 min was found to be effective for the complete removal of the PC shell. Fluorescence microscopy images of an etched edge of a $Cs_4CdBi_2Cl_{12}$:Mn-PC fiber are shown in Figure S15c. As evident from the FM images, the removal of the PC cladding results in a more than 3-fold reduction in fiber diameter. In contrast to the unetched part of the fiber, which has a significant nonemissive PC cladding, the etched fiber exhibits uniform light emission throughout its body. Fluorescence microscopy images also revealed that the etched fibers have a relatively uniform diameter. The etched fibers were collected and used for fabric weaving. Scintillation fabrics were prepared using $Cs_3Cu_2I_5$-PC and $Cs_4CdBi_2Cl_{12}$:Mn-PC fibers. Digital images of the obtained fabrics under visible light and X-ray

irradiation are shown in Figure 3b. The uniform color of the woven scintillation fabrics under both visible light and X-ray irradiation supports their compositional homogeneity. The woven scintillation fabrics show almost no inactive gaps between the adjacent fibers. The resulting scintillation fabrics exhibit flexibility and can be reversibly bent, twisted, and stretched (Figure S16). When the deformation force is removed, the woven scintillator returns to its original shape. It is noteworthy that scintillators with the flexibility of a textile would be of considerable interest for X-ray imaging of intricate objects. Such scintillator fabrics would make it possible to wrap objects with complex shapes or to create wearable scintillator textiles for conformal X-ray imaging. X-ray scintillation fabrics with such flexibility can be made by knitting, as knitted structures typically exhibit significantly improved flexibility compared to woven structures.[58]

A third approach for fabricating nonplanar X-ray scintillators involves assembling scintillation fibers. Cladding-free etched scintillation fibers were used because of their superior flexibility. Hemispherical X-ray scintillators were fabricated by simply assembling a single layer of scintillation fibers onto a plastic hemisphere. The resulting structures were secured with polypropylene tape. While fiber-assembled scintillators are not

as robust as 3D-printed or woven scintillators, their ease of fabrication and adaptability to objects of various shapes make them interesting for certain applications (SI, section 16).

Figure 4 shows the results of X-ray imaging obtained using 3D-printed and planar $Cs_3Cu_2I_5$-PC scintillators. A metal hemisphere with circular holes served as the imaging object (Figure S17a-b). Camera 1 was positioned directly in front of the scintillator (i.e., the X-ray source, scintillator, and camera 1 were aligned), while camera 2 was positioned at an angle of ~65° from the line connecting the X-ray source and the scintillator. The images produced by the planar and 3D $Cs_3Cu_2I_5$-PC scintillators shared common characteristics, but also exhibited notable differences. Although the dimensions of the planar scintillator were sufficient to cover the entire object, small sections of the object were missing from the top and bottom of the X-ray images. This is due to the 2D projection imaging used with a planar scintillator, which results in significantly exaggerated dimensions, compared with the actual object size. In addition, if the object has a complex 3D structure, the images are inevitably distorted (Figure 4a). The frontal image captured by camera 1 was almost identical to that obtained with the 3D scintillator, except for the exaggerated dimensions and distorted image of the object. Crucially, as expected, imaging from different perspectives with the planar scintillator does not provide additional information. Instead, changing the viewing angle simply results in an even more distorted image of the object (Figure 4a). Similar patterns would result from imaging of a flat circular metal plate with holes. On the other hand, due to the 2D nature of the image, certain specific components of the object cannot be precisely located. However, this type of information is critical for medical diagnostics, treatment, and materials inspection.

Contrary to the planar scintillator, conformal X-ray imaging with the 3D scintillator enabled the acquisition of more precise information regarding the object's dimensions, shape, and position. As shown in Figure 4b, the X-ray images obtained with the 3D scintillator successfully depicted the entire object. The frontal image captured by camera 1 displays the object without any distortion, while the image obtained by camera 2 provides a side view, clearly revealing even the object's end border. In this case, the 3D scintillator facilitated the acquisition of novel and valuable information about the object from a different perspective, which is not possible with a planar scintillator. The image from camera 2 clearly shows the circular holes located near the end of the object, while these elements remain indistinguishable in the images obtained with the planar scintillator. Thus, conformal X-ray imaging employing a 3D scintillator and multiple cameras positioned at varying viewing angles enables the acquisition of accurate data on the size, spatial location, and shape of an object. In addition, because the images obtained from different perspectives are complementary, they can be used to reconstruct a 3D model of the object. Such insights are unattainable with flat scintillation screens, unless the object is repositioned relative to the scintillator/X-ray source and X-ray images are captured. However, this would necessitate repeated exposure of the object to X-rays, and the resulting distorted X-ray images would preclude reconstruction of the true shape of the object.

We also investigated the potential of woven scintillator fabrics for X-ray imaging. Figure 5 shows X-ray images generated by using a planar $Cs_4CdBi_2Cl_{12}$:Mn-PC scintillator and a woven $Cs_4CdBi_2Cl_{12}$:Mn-PC flexible scintillator. A V-shaped metal plate served as the imaging object (Figures S17c

and S17d). Despite the uniform width of the object along its entire length, the images obtained with the planar $Cs_4CdBi_2Cl_{12}$:Mn-PC scintillator showed significant distortion. The width of the object appeared to increase with increasing distance from the center in both the left and right directions. In addition, acquiring images from different viewing angles did not provide any information about the true 3D shape or spatial position of the object. Similar X-ray images could be produced by imaging a straight metal plate with varying dimensions along its length. This further demonstrates the limitations of planar scintillators in accurately and reliably imaging objects with nonplanar or irregular 3D geometries. Because of its flexibility, the woven $Cs_4CdBi_2Cl_{12}$:Mn-PC scintillator was easily wrapped around the object, giving it a shape similar to that of the object itself. The images generated with the woven scintillator revealed the shape of the object with near-perfect accuracy (see Figure 5b, as well as Figures S17c and S17d). There was no noticeable distortion in the images, and the dimensions of the object accurately reflected its actual size. This achievement can be attributed to the flexibility of the woven scintillator, which allowed it to conform to the shape of the object and eliminate extraneous optical effects that cause image distortion. In addition, similar to the 3D-printed scintillators, the images captured by Camera 1 and Camera 2 not only provided accurate dimensional information but also allowed the reconstruction of the actual shape of the object. Comparable results were obtained with a woven $Cs_3Cu_2I_5$-PC scintillator fabric (Figure S18). We also used 3D scintillators produced through fiber assembling for conformal X-ray imaging. The results showed that these custom-built 3D scintillators can provide detailed information about nonflat 3D objects (Figures S19−S21).

In summary, we have demonstrated scalable strategies for the production of multimaterial luminescent fibers containing nanoemitters with emission wavelengths ranging from 400 to 700 nm. We used these luminescent fibers for the realization of 3D conformal X-ray scintillation screens using additive manufacturing, fabric weaving, and fiber assembling. Thermal drawing of macroscopic polycarbonate preforms doped with X-ray active materials such as $Cs_3Cu_2I_5$ nanoparticles, Cu_2I_2-nanoclusters, and $Cs_4CdBi_2Cl_{12}$:Mn microcrystals led to uniform composite fibers emitting within the blue, green, and red wavelengths of the optical spectrum, respectively. The dimensions and structure of the scintillation fibers were optimized to make them suitable for additive manufacturing and woven fabric production. Multilayered scintillation fibers were utilized as filaments to successfully print 3D scintillators with intricate shapes. Thin cladding-free fibers were integrated into scintillation fabrics that have a solid and flexible structure, enabling conformal X-ray imaging of nonplanar objects. Conformal X-ray imaging with the 3D-printed and woven flexible scintillators revealed that they provide much more detailed and reliable information about the structure, shape, and dimensions, compared to planar scintillators. The ability to produce 3D scintillation screens of complicated shapes is vital for medical examinations, therapy, and materials inspection. This allows for the creation of scintillation screens that match the unique contours of the human body for accurate X-ray imaging. Our work paves the way for nonflat custom-fit scintillators for radiation imaging applications, as well as applications in large-area high-energy radiation and particle detection.

EXPERIMENTAL SECTION

Preparation of Composite Films. PC-based composite films with an active material content of 10% by weight were prepared by drop-casting and/or blade-coating techniques, as described in detail in the SI.

Preform Preparation for Fibers Designed for 3D Printing. For preform preparation, pure PC and the composite films were kept under vacuum conditions for several hours. Pure PC film was rolled onto a Teflon PFA film-covered metal rod (6 mm in diameter) until its diameter reached 24 mm. Subsequently, the composite film (6 cm × 28 cm) was placed on a pure PC film and rolled onto the rod. After that, several layers of pure PC were rolled onto the rod. This process resulted in an increase in the diameter from 24 mm to 26 mm. The preform was then covered with Teflon tape and kept under vacuum at 120 °C for 3−4 h. Subsequently, under vacuum conditions, the temperature was increased from 120 °C to 186 °C and the preform was consolidated for 40 min. This process resulted in a uniform solid preform. Schematic illustrations for the preform preparation procedures, preform structure, and photographs of a consolidated Cu_2I_2-PC preform are shown in Figures S5a and S5b.

Preform Preparation for Fibers Designed for Fabric Weaving. Composite films with a width of 6 cm and a total length of 30 cm were used for preform preparation. After degassing under vacuum at 120 °C for 3−4 h, the composite film was rolled onto a Teflon PFA-covered metal rod with a diameter of 6 mm. Then several layers of PVDF film were rolled onto the rod. Subsequently, PC film was rolled onto the PVDF layer, resulting in a total diameter of 20 mm. The preform was then covered with Teflon tape and kept under vacuum at 120 °C for 3−4 h. After that, under vacuum conditions, the temperature was increased from 120 to 186 °C and the preform was consolidated for 40 min. A schematic illustration of the preform preparation procedures and preform structure is shown in Figure S5c.

Fiber Drawing. A custom-built fiber drawing system was used to produce multimaterial scintillation fibers (Figure S6). For a typical fiber drawing, a consolidated preform is attached to the downfeed system, and the furnace temperature is slowly increased from room temperature to 240 °C. Once the drawing process begins, the capstan speed, furnace temperature, and preform feed (downfeed) speed are controlled to get fibers of the required diameters ranging from 200 to 2000 μm. Table S1 summarizes the optimized fiber drawing parameters and the dependence of the fiber diameter on the drawing conditions.

ASSOCIATED CONTENT

ⓢ Supporting Information

The Supporting Information is available free of charge at https://pubs.acs.org/doi/10.1021/acsmaterialslett.3c01359.

> Materials synthesis and characterization, X-ray attenuation efficiency calculation, determination of the light yield, experimental methods, preform and fiber production details, fiber characterization (cross-section analysis, X-ray resolution, and optical characterization), details of additive manufacturing of X-ray scintillators, production details of woven scintillation fabrics, images of the objects used for conformal X-ray imaging (PDF)

> Production of composite scintillation fibers doped with nanoemitters (Video S1) (AVI)

> 3D printing of conformal X-ray scintillation screens (Video S2) (AVI)

AUTHOR INFORMATION

Corresponding Authors

Osman M. Bakr − *KAUST Catalysis Center (KCC), Division of Physical Sciences and Engineering, King Abdullah University of Science and Technology (KAUST), Thuwal 23955−6900, Saudi Arabia;* ⓞ orcid.org/0000-0002-3428-1002; Email: osman.bakr@kaust.edu.sa

Mehmet Bayindir − *Center for Hybrid Nanostructures, University of Hamburg, Hamburg 22761, Germany;* ⓞ orcid.org/0000-0003-0233-6870; Email: mehmet.bayindir@uni-hamburg.de

Authors

Bedil M. Saidzhonov − *KAUST Catalysis Center (KCC), Division of Physical Sciences and Engineering, King Abdullah University of Science and Technology (KAUST), Thuwal 23955−6900, Saudi Arabia;* ⓞ orcid.org/0000-0001-7773-6524

Khursand E. Yorov − *KAUST Catalysis Center (KCC), Division of Physical Sciences and Engineering, King Abdullah University of Science and Technology (KAUST), Thuwal 23955−6900, Saudi Arabia;* ⓞ orcid.org/0000-0002-7523-3410

Peng Yuan − *KAUST Catalysis Center (KCC), Division of Physical Sciences and Engineering, King Abdullah University of Science and Technology (KAUST), Thuwal 23955−6900, Saudi Arabia*

Saidkhodzha Nematulloev − *KAUST Catalysis Center (KCC), Division of Physical Sciences and Engineering, King Abdullah University of Science and Technology (KAUST), Thuwal 23955−6900, Saudi Arabia*

Azimet Akber Karluk − *KAUST Catalysis Center (KCC), Division of Physical Sciences and Engineering, King Abdullah University of Science and Technology (KAUST), Thuwal 23955−6900, Saudi Arabia*

Taimoor Ahmad − *KAUST Catalysis Center (KCC), Division of Physical Sciences and Engineering, King Abdullah University of Science and Technology (KAUST), Thuwal 23955−6900, Saudi Arabia*

Omar F. Mohammed − *Advanced Membranes and Porous Materials Center, Division of Physical Science and Engineering, King Abdullah University of Science and Technology (KAUST), Thuwal 23955-6900, Saudi Arabia;* ⓞ orcid.org/0000-0001-8500-1130

Complete contact information is available at:
https://pubs.acs.org/10.1021/acsmaterialslett.3c01359

Author Contributions

CRediT: **Bedil M. Saidzhonov** conceptualization, formal analysis, investigation, methodology, data curation, validation, visualization, writing-original draft, writing-review & editing; **Khursand E. Yorov** data curation, investigation, methodology; **Peng Yuan** investigation, methodology; **Saidkhodzha Nematulloev** investigation, methodology; **Azimet A. Karluk** investigation, methodology; **Taimoor Ahmad** investigation, methodology; **Omar F. Mohammed** writing-review & editing; **Osman M. Bakr** funding acquisition, investigation, methodology, project administration, resources, supervision, validation, writing-review & editing; **Mehmet Bayindir** conceptual-

ization, formal analysis, funding acquisition, investigation, methodology, project administration, supervision, validation, visualization, writing-original draft, writing-review & editing.

Notes

The authors declare the following competing financial interest(s): O.M.B. is a founder of Quantum Solutions, a company that develops optoelectronic devices.

REFERENCES

(1) Bayindir, M.; Sorin, F.; Abouraddy, A. F.; Viens, J.; Hart, S. D.; Joannopoulos, J. D.; Fink, Y. Metal-Insulator-Semiconductor Opto-electronic Fibres. *Nature* **2004**, *431*, 826−829.

(2) Abouraddy, A. F.; Bayindir, M.; Benoit, G.; Hart, S. D.; Kuriki, K.; Orf, N.; Shapira, O.; Sorin, F.; Temelkuran, B.; Fink, Y. Towards Multimaterial Multifunctional Fibres That See, Hear, Sense and Communicate. *Nat. Mater.* **2007**, *6*, 336−347.

(3) Khudiyev, T.; Tobail, O.; Bayindir, M. Tailoring Self-Organized Nanostructured Morphologies in Kilometer-Long Polymer Fiber. *Sci. Rep.* **2014**, *4*, 1−8.

(4) Yaman, M.; Khudiyev, T.; Ozgur, E.; Kanik, M.; Aktas, O.; Ozgur, E. O.; Deniz, H.; Korkut, E.; Bayindir, M. Arrays of Indefinitely Long Uniform Nanowires and Nanotubes. *Nat. Mater.* **2011**, *10*, 494−501.

(5) Kanik, M.; Aktas, O.; Sen, H. S.; Durgun, E.; Bayindir, M. Spontaneous High Piezoelectricity in Poly(Vinylidene Fluoride) Nanoribbons Produced by Iterative Thermal Size Reduction Technique. *ACS Nano* **2014**, *8*, 9311−9323.

(6) Yan, W.; Noel, G.; Loke, G.; Meiklejohn, E.; Khudiyev, T.; Marion, J.; Rui, G.; Lin, J.; Cherston, J.; Sahasrabudhe, A.; Wilbert, J.; Wicaksono, I.; Hoyt, R. W.; Missakian, A.; Zhu, L.; Ma, C.; Joannopoulos, J.; Fink, Y. Single Fibre Enables Acoustic Fabrics via Nanometre-Scale Vibrations. *Nature* **2022**, *603*, 616−623.

(7) Canales, A.; Jia, X.; Froriep, U. P.; Koppes, R. A.; Tringides, C. M.; Selvidge, J.; Lu, C.; Hou, C.; Wei, L.; Fink, Y.; Anikeeva, P. Multifunctional Fibers for Simultaneous Optical, Electrical and Chemical Interrogation of Neural Circuits in Vivo. *Nat. Biotechnol.* **2015**, *33*, 277−284.

(8) Ozgur, E.; Aktas, O.; Kanik, M.; Yaman, M.; Bayindir, M. Macroscopic Assembly of Indefinitely Long and Parallel Nanowires into Large Area Photodetection Circuitry. *Nano Lett.* **2012**, *12*, 2483−2487.

(9) Kanik, M.; Orguc, S.; Varnavides, G.; Kim, J.; Benavides, T.; Gonzalez, D.; Akintilo, T.; Tasan, C. C.; Chandrakasan, A. P.; Fink, Y.; Anikeeva, P. Strain-Programmable Fiber-Based Artificial Muscle. *Science* **2019**, *365*, 145−150.

(10) Sahasrabudhe, A.; Rupprecht, L. E.; Orguc, S.; Khudiyev, T.; Tanaka, T.; Sands, J.; Zhu, W.; Tabet, A.; Manthey, M.; Allen, H.; Loke, G.; Antonini, M.-J.; Rosenfeld, D.; Park, J.; Garwood, I. C.; Yan, W.; Niroui, F.; Fink, Y.; Chandrakasan, A.; Bohórquez, D. V.; Anikeeva, P. Multifunctional Microelectronic Fibers Enable Wireless Modulation of Gut and Brain Neural Circuits. *Nat. Biotechnol.* **2023**, DOI: 10.1038/s41587-023-01833-5.

(11) Yaffe, M. J.; Rowlands, J. A. X-ray Detectors for Digital Radiography. *Phys. Med. Biol.* **1997**, *42*, 1−39.

(12) Hanke, R.; Fuchs, T.; Uhlmann, N. X-Ray Based Methods for Non-Destructive Testing and Material Characterization. *Nucl. Instrum. Methods Phys. Res., Sect. A* **2008**, *591*, 14−18.

(13) Ou, X.; Chen, X.; Xu, X.; Xie, L.; Chen, X.; Hong, Z.; Bai, H.; Liu, X.; Chen, Q.; Li, L.; Yang, H. Recent Development in X-Ray Imaging Technology: Future and Challenges. *Research* **2021**, *2021*, DOI: 10.34133/2021/9892152.

(14) Zhou, Y.; Chen, J.; Bakr, O. M.; Mohammed, O. F. Metal Halide Perovskites for X-ray Imaging Scintillators and Detectors. *ACS Energy Lett.* **2021**, *6*, 739−768.

(15) Olivo, A.; Chana, D.; Speller, R. A Preliminary Investigation of the Potential of Phase Contrast X-ray Imaging in the Field of Homeland Security. *J. Phys. D: Appl. Phys.* **2008**, *41*, 225503.

(16) Sakhatskyi, K.; Turedi, B.; Matt, G. J.; Wu, E.; Sakhatska, A.; Bartosh, V.; Lintangpradipto, M. N.; Naphade, R.; Shorubalko, I.; Mohammed, O. F.; Yakunin, S.; Bakr, O. M.; Kovalenko, M. V. Stable Perovskite Single-Crystal X-ray Imaging Detectors with Single-Photon Sensitivity. *Nat. Photonics* **2023**, *17*, 510−517.

(17) van Eijk, C. W. E. Inorganic Scintillators in Medical Imaging. *Phys. Med. Biol.* **2002**, *47*, R85−R106.

(18) Wang, Y.; Zhang, Q. A Characterization Study on Perovskite X-ray Detector Performance Based on a Digital Radiography System. *Nucl. Sci. Technol.* **2023**, *34*, 1−11.

(19) Shao, W.; Wang, X.; Zhang, Z.; Huang, J.; Han, Z.; Pi, S.; Xu, Q.; Zhang, X.; Xia, X.; Liang, H.; Shao, W.; Zhang, Z.; Han, Z.; Pi, S.; Xia, X.; Liang, H.; Wang, X.; Zhang, X.; Huang, J.; Xu, Q. Highly Efficient and Flexible Scintillation Screen Based on Manganese(II) Activated 2D Perovskite for Planar and Nonplanar High-Resolution X-ray Imaging. *Adv. Opt. Mater.* **2022**, *10*, 2102282.

(20) Moses, W. W. Scintillator Requirements for Medical Imaging. In *Proceedings of the International Conference on Inorganic Scintillators and Their Applications: SCINT99*; 1999. LBNL-4580. Available via the Internet at: https://escholarship.org/uc/item/5pc245ds.

(21) Zhu, W.; Ma, W.; Su, Y.; Chen, Z.; Chen, X.; Ma, Y.; Bai, L.; Xiao, W.; Liu, T.; Zhu, H.; Liu, X.; Liu, H.; Liu, X.; Yang, Y. (Michael). Low-Dose Real-Time X-ray Imaging with Nontoxic Double Perovskite Scintillators. *Light. Sci. Appl.* **2020**, *9*, 112.

(22) Lecoq, P. Development of New Scintillators for Medical Applications. *Nucl. Instrum. Methods Phys. Res., Sect. A* **2016**, *809*, 130−139.

(23) Cao, F.; Yu, D.; Ma, W.; Xu, X.; Cai, B.; Yang, Y. M.; Liu, S.; He, L.; Ke, Y.; Lan, S.; Choy, K.-L.; Zeng, H. Shining Emitter in a Stable Host: Design of Halide Perovskite Scintillators for X-ray Imaging from Commercial Concept. *ACS Nano* **2020**, *14*, 5183−5193.

(24) Nagarkar, V. V.; Miller, S. R.; Tipnis, S. V.; Lempicki, A.; Brecher, C.; Lingertat, H. A New Large Area Scintillator Screen for X-Ray Imaging. *Nucl. Instrum. Methods Phys. Res., Sect. B* **2004**, *213*, 250−254.

(25) Kuo, T.-T.; Wu, C.-M.; Lu, H.-H.; Chan, I.; Wang, K.; Leou, K.-C. Flexible X-ray Imaging Detector Based on Direct Conversion in Amorphous Selenium. *J. Vac. Sci. Technol., A* **2014**, *32*, 41507.

(26) van Breemen, A. J. J. M.; Simon, M.; Tousignant, O.; Shanmugam, S.; van der Steen, J. L.; Akkerman, H. B.; Kronemeijer, A.; Ruetten, W.; Raaijmakers, R.; Alving, L.; Jacobs, J.; Malinowski, P. E.; De Roose, F.; Gelinck, G. H. Curved Digital X-ray Detectors. *npj Flex. Electron.* **2020**, *4*, 22.

(27) Cao, C. F.; Ma, K. L.; Shan, H.; Liu, T. F.; Zhao, S. Q.; Wan, Y.; Jun-Zhang; Wang, H. Q. CT Scans and Cancer Risks: A Systematic Review and Dose-Response Meta-Analysis. *BMC Cancer* **2022**, *22*, 1−13.

(28) Zhou, Y.; Wang, X.; He, T.; Yang, H.; Yang, C.; Shao, B.; Gutiérrez-Arzaluz, L.; Bakr, O. M.; Zhang, Y.; Mohammed, O. F. Large-Area Perovskite-Related Copper Halide Film for High-Resolution Flexible X-ray Imaging Scintillation Screens. *ACS Energy Lett.* **2022**, *7*, 844−846.

(29) Chen, W.; Zhou, M.; Liu, Y.; Yu, X.; Pi, C.; Yang, Z.; Zhang, H.; Liu, Z.; Wang, T.; Qiu, J.; Yu, S. F.; Yang, Y.; Xu, X. All-Inorganic Perovskite Polymer-Ceramics for Flexible and Refreshable X-ray Imaging. *Adv. Funct. Mater.* **2022**, *32*, 2107424.

(30) Lian, L.; Wang, X.; Zhang, P.; Zhu, J.; Zhang, X.; Gao, J.; Wang, S.; Liang, G.; Zhang, D.; Gao, L.; Song, H.; Chen, R.; Lan, X.; Liang, W.; Niu, G.; Tang, J.; Zhang, J. Highly Luminescent Zero-Dimensional Organic Copper Halides for X-Ray Scintillation. *J. Phys. Chem. Lett.* **2021**, *12*, 6919−6926.

(31) Zhang, F.; Zhou, Y.; Chen, Z.; Wang, M.; Ma, Z.; Chen, X.; Jia, M.; Wu, D.; Xiao, J.; Li, X.; Zhang, Y.; Shi, Z.; Shan, C. Thermally Activated Delayed Fluorescence Zirconium-Based Perovskites for Large-Area and Ultraflexible X-Ray Scintillator Screens. *Adv. Mater.* **2022**, *34*, 2204801.

(32) Zhao, J.; Zhao, L.; Deng, Y.; Xiao, X.; Ni, Z.; Xu, S.; Huang, J. Perovskite-Filled Membranes for Flexible and Large-Area Direct-Conversion X-Ray Detector Arrays. *Nat. Photonics* **2020**, *14*, 612–617.

(33) Koshimizu, M. Recent Progress of Organic Scintillators. *Jpn. J. Appl. Phys.* **2023**, *62*, 010503.

(34) Morishita, Y.; Di Fulvio, A.; Clarke, S. D.; Kearfott, K. J.; Pozzi, S. A. Organic Scintillator-Based Alpha/Beta Detector for Radiological Decontamination. *Nucl. Instrum. Methods Phys. Res., Sect. A* **2019**, *935*, 207–213.

(35) Ma, W.; Su, Y.; Zhang, Q.; Deng, C.; Pasquali, L.; Zhu, W.; Tian, Y.; Ran, P.; Chen, Z.; Yang, G.; Liang, G.; Liu, T.; Zhu, H.; Huang, P.; Zhong, H.; Wang, K.; Peng, S.; Xia, J.; Liu, H.; Liu, X.; Yang, Y. M. Thermally Activated Delayed Fluorescence (TADF) Organic Molecules for Efficient X-Ray Scintillation and Imaging. *Nat. Mater.* **2022**, *21*, 210–216.

(36) Du, X.; Zhao, S.; Wang, L.; Wu, H.; Ye, F.; Xue, K.-H.; Peng, S.; Xia, J.; Sang, Z.; Zhang, D.; Xiong, Z.; Zheng, Z.; Xu, L.; Niu, G.; Tang, J. Efficient and Ultrafast Organic Scintillators by Hot Exciton Manipulation. *Nat. Photonics* **2024**, *18*, 162–169.

(37) Li, P.; Zhou, Z.; Zhao, Y. S.; Yan, Y. Recent Advances in Luminescent Metal-Organic Frameworks and Their Photonic Applications. *Chem. Commun.* **2021**, *57*, 13678–13691.

(38) Wang, J.-X.; Wang, Y.; Almalki, M.; Yin, J.; Shekhah, O.; Jia, J.; Gutiérrez-Arzaluz, L.; Cheng, Y.; Alkhazragi, O.; Maka, V. K.; Ng, T. K.; Bakr, O. M.; Ooi, B. S.; Eddaoudi, M.; Mohammed, O. F. Engineering Metal-Organic Frameworks with Tunable Colors for High-Performance Wireless Communication. *J. Am. Chem. Soc.* **2023**, *145*, 15435–15442.

(39) Perego, J.; Villa, I.; Pedrini, A.; Padovani, E. C.; Crapanzano, R.; Vedda, A.; Dujardin, C.; Bezuidenhout, C. X.; Bracco, S.; Sozzani, P. E.; Comotti, A.; Gironi, L.; Beretta, M.; Salomoni, M.; Kratochwil, N.; Gundacker, S.; Auffray, E.; Meinardi, F.; Monguzzi, A. Composite Fast Scintillators Based on High-Z Fluorescent Metal-Organic Framework Nanocrystals. *Nat. Photonics* **2021**, *15*, 393–400.

(40) Orfano, M.; Perego, J.; Cova, F.; Bezuidenhout, C. X.; Piva, S.; Dujardin, C.; Sabot, B.; Pierre, S.; Mai, P.; Daniel, C.; Bracco, S.; Vedda, A.; Comotti, A.; Monguzzi, A. Efficient Radioactive Gas Detection by Scintillating Porous Metal-Organic Frameworks. *Nat. Photonics* **2023**, *17*, 672–678.

(41) Mann, S. E.; Schooneveld, E. M.; Rhodes, N. J.; Liu, D.; Sykora, G. J. Timing Properties of Radioluminescence in Nanoparticle ZnS:Ag Scintillators. *Opt. Mater.: X* **2023**, *17*, 100226.

(42) Gupta, S. K.; Zuniga, J. P.; Abdou, M.; Thomas, M. P.; De Alwis Goonatilleke, M.; Guiton, B. S.; Mao, Y. Lanthanide-Doped Lanthanum Hafnate Nanoparticles as Multicolor Phosphors for Warm White Lighting and Scintillators. *Chem. Eng. J.* **2020**, *379*, 122314.

(43) Villa, I.; Moretti, F.; Fasoli, M.; Rossi, A.; Hattendorf, B.; Dujardin, C.; Niederberger, M.; Vedda, A.; Lauria, A. The Bright X-ray Stimulated Luminescence of HfO2 Nanocrystals Activated by Ti Ions. *Adv. Opt. Mater.* **2020**, *8*, 1901348.

(44) Cooper, D. R.; Capobianco, J. A.; Seuntjens, J. Radio-luminescence Studies of Colloidal Oleate-Capped β-Na(Gd,Lu)-F4:Ln³⁺ Nanoparticles (Ln = Ce, Eu, Tb). *Nanoscale* **2018**, *10*, 7821–7832.

(45) Lian, L.; Zheng, M.; Zhang, W.; Yin, L.; Du, X.; Zhang, P.; Zhang, X.; Gao, J.; Zhang, D.; Gao, L.; Niu, G.; Song, H.; Chen, R.; Lan, X.; Tang, J.; Zhang, J. Efficient and Reabsorption-Free Radioluminescence in Cs3Cu2I5 Nanocrystals with Self-Trapped Excitons. *Adv. Sci.* **2020**, *7*, 2000195.

(46) Zhou, Y.; Wang, X.; He, T.; Yang, H.; Yang, C.; Shao, B.; Gutiérrez-Arzaluz, L.; Bakr, O. M.; Zhang, Y.; Mohammed, O. F. Large-Area Perovskite-Related Copper Halide Film for High-Resolution Flexible X-Ray Imaging Scintillation Screens. *ACS Energy Lett.* **2022**, *7*, 844–846.

(47) Busch, J. M.; Zink, D. M.; Di Martino-Fumo, P.; Rehak, F. R.; Boden, P.; Steiger, S.; Fuhr, O.; Nieger, M.; Klopper, W.; Gerhards, M.; Bräse, S. Highly Soluble Fluorine Containing Cu(I) AlkylPyrPhos TADF Complexes. *Dalton Trans.* **2019**, *48*, 15687–15698.

(48) Vargas, B.; Reyes-Castillo, D. T.; Coutino-Gonzalez, E.; Sánchez-Aké, C.; Ramos, C.; Falcony, C.; Solis-Ibarra, D. Enhanced Luminescence and Mechanistic Studies on Layered Double-Perovskite Phosphors: Cs4Cd1−xMnxBi2Cl12. *Chem. Mater.* **2020**, *32*, 9307–9315.

(49) Holzapfel, N. P.; Majher, J. D.; Strom, T. A.; Moore, C. E.; Woodward, P. M. Cs4Cd1-XMnxBi2Cl12- A Vacancy-Ordered Halide Perovskite Phosphor with High-Efficiency Orange-Red Emission. *Chem. Mater.* **2020**, *32*, 3510–3516.

(50) Yuan, P.; He, T.; Zhou, Y.; Yin, J.; Zhang, H.; Zhang, Y.; Yuan, X.; Dong, C.; Huang, R.; Shao, W.; Chen, S.; Song, X.; Zhou, R.; Zheng, N.; Abulikemu, M.; Eddaoudi, M.; Bayindir, M.; Mohammed, O. F.; Bakr, O. M. Hybrid Thermally Activated Nanocluster Fluorophores for X-Ray Scintillators. *ACS Energy Lett.* **2023**, *8*, 5088–5097.

(51) Goswami, N.; Yao, Q.; Luo, Z.; Li, J.; Chen, T.; Xie, J. Luminescent Metal Nanoclusters with Aggregation-Induced Emission. *J. Phys. Chem. Lett.* **2016**, *7*, 962–975.

(52) Zink, D. M.; Volz, D.; Baumann, T.; Mydlak, M.; Flügge, H.; Friedrichs, J.; Nieger, M.; Bräse, S. Heteroleptic, Dinuclear Copper(I) Complexes for Application in Organic Light-Emitting Diodes. *Chem. Mater.* **2013**, *25*, 4471–4486.

(53) Gibson, I.; Rosen, D. W.; Stucker, B. *Additive Manufacturing Technologies: Rapid Prototyping to Direct Digital Manufacturing*; Springer, 2010. DOI: 10.1007/978-1-4419-1120-9.

(54) *Fused Deposition Modeling: Most Common 3D Printing Method*. https://www.livescience.com/39810-fused-deposition-modeling.html (accessed July 9, 2023).

(55) Odedra, D.; Narayanasamy, S.; Sabongui, S.; Priya, S.; Krishna, S.; Sheikh, A. Dual Energy CT Physics—A Primer for the Emergency Radiologist. *Front. Radiol.* **2022**, *276*, 637–653.

(56) Shao, W.; He, T.; Wang, J. X.; Zhou, Y.; Yuan, P.; Wu, W.; Zhang, Z.; Bakr, O. M.; Liang, H.; Mohammed, O. F. Transparent Organic and Metal Halide Tandem Scintillators for High-Resolution Dual-Energy X-Ray Imaging. *ACS Energy Lett.* **2023**, *8*, 2505–2512.

(57) Zeng, W.; Shu, L.; Li, Q.; Chen, S.; Wang, F.; Tao, X.-M. Fiber-Based Wearable Electronics: A Review of Materials, Fabrication, Devices, and Applications. *Adv. Mater.* **2014**, *26*, 5310–5336.

(58) Ismar, E.; Kurşun Bahadir, S.; Kalaoglu, F.; Koncar, V. Futuristic Clothes: Electronic Textiles and Wearable Technologies. *Global Challenges* **2020**, *4*, 1900092.